Journal Pre-proof

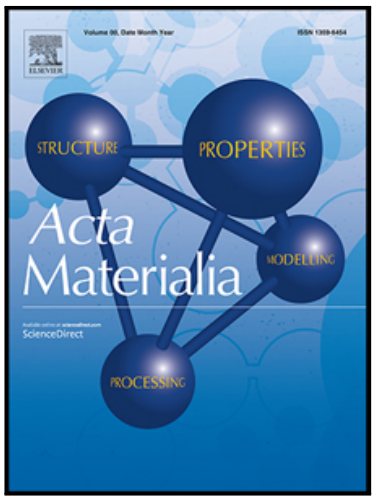

Ultrasonic-vibration-enhanced plasticity of an entropic alloy at room temperature

Zhen Li , Xin Li , Zhiyuan Huang , Zhenxuan Zhang , Xiong Liang , Huan Liu , Peter K. Liaw , Jiang Ma , Jun Shen

PII: S1359-6454(21)00947-2
DOI: https://doi.org/10.1016/j.actamat.2021.117569
Reference: AM 117569

To appear in: *Acta Materialia*

Received date: 26 September 2021
Revised date: 28 November 2021
Accepted date: 19 December 2021

Please cite this article as: Zhen Li , Xin Li , Zhiyuan Huang , Zhenxuan Zhang , Xiong Liang , Huan Liu , Peter K. Liaw , Jiang Ma , Jun Shen , Ultrasonic-vibration-enhanced plasticity of an entropic alloy at room temperature, *Acta Materialia* (2021), doi: https://doi.org/10.1016/j.actamat.2021.117569

Ultrasonic-vibration-enhanced plasticity of an entropic alloy at room temperature

Zhen Li[a,b,c], Xin Li[a], Zhiyuan Huang[a], Zhenxuan Zhang[a], Xiong Liang[a], Huan Liu[d], Peter K. Liaw[e,*] pliaw@utk.edu, Jiang Ma[a,*] majiang@szu.edu.cn, and Jun Shen[a]

[a]College of Mechatronics and Control Engineering, Shenzhen University, Shenzhen 518060, China

[b]College of Physics and Optoelectronic Engineering, Shenzhen University, Shenzhen 518060, China

[c]Department of Mechanics and Aerospace Engineering, Southern University of Science and Technology, Shenzhen, 518055, China

[d]College of Mechanics and Materials, Hohai University, Nanjing, 210000, China

[e]Department of Materials Science and Engineering, The University of Tennessee, Knoxville, TN 37996, USA

[*]To whom correspondence should be addressed

Abstract

Deformation at a high-strain rate and low stress is of great significance for the emerging entropic alloys. However, this deformation process is generally achieved under heating or cryogenic conditions to ensure a good plasticity. Here, we demonstrate a facile route to enhance the plasticity of entropic alloys at ambient temperature. Assisted by ultrasonic vibration at a frequency of 20,000 Hz, the compression strain of the $Al_{80}Li_5Mg_5Zn_5Cu_5$ entropic alloy increases from 17% under conventional

compression to 30% within 1 s, while the applied stress is less than 100 MPa, only 1/6 of the compressive strength. In contrast to conventional compression, the ultrasonic loading achieves a high-instantaneous strain rate up to 10^3 s^{-1} and high-frequency cyclic loading. This loading mode results in reflected stress waves and stress-relief effects in the deformation areas, thus causing the dislocations diffusion in face-centered-cubic (FCC) phases as well as the refinement and dispersion of intermetallic phases in the entropic alloy. These distinct microstructural evolutions synchronously suppress dislocations pile-up, and facilitate the grains rotation and sub-grains formation, which significantly decrease the deformation stresses, accommodate higher plastic strains, and eliminate deformation textures. Our studies discover a novel deformation mechanism for the entropic alloy that can offer a versatile approach of rapid structure forming.

Keywords

Entropic alloy; Ultrasonic vibration loading; Enhanced plasticity; Dynamic deformation mechanism; Microstructures evolution

1. Introduction

A series of entropic alloys, especially high-entropy alloys (HEAs) and their derivatives, have been developed, based on the concept of multi-principal elements [1, 2]. These entropic alloys have been emerging as excellent structural and functional materials with flexible compositions, and unique properties like high strength, great corrosion resistance, anti-irradiation, and extreme-temperature tolerance, etc. [3-7] Forming entropic alloys into desired structures are critical for different applications.

Therefore, the approaches to achieve enhanced plasticity and rapid deformation of the alloys are greatly concerned.

As solid solutions of multiple elements, entropic alloys may exhibit distinct deformation mechanisms, compared to conventional alloys [8-11]. The mechanical properties and deformation behaviors have been widely studied under different loading conditions. A variety of entropic-alloy samples have been subjected to the conventional tension and compression tests at a strain rate of $10^{-4} \sim 10^{3}$ s^{-1}, under ambient temperature [12]. In general, the HEA systems with a principal phase of a face-centered-cubic (FCC) structure possess the good synergy of mechanical strength and ductility, while the increase of a body-centered-cubic (BCC) phase is conducive to achieving high yield strength. The entropic alloys with more compositions tend to be improved in strength at the expense of ductility, due to solid-solution strengthening [5, 13]. To reconcile this contradiction, it has been proposed to tune the precipitates distribution and valence electron concentration (VEC) by doping elements in HEAs [14], which can further influence the phase proportions and ductility. Moreover, the loading tests under elevated-temperature or cryogenic conditions were also carried out to improve the deformation capacity of entropic alloys. Most of the entropic alloys exhibited lower strength and better plasticity at 1,000 ~ 1,500 K dominated by grain sliding [5, 15] or ultra-low temperatures (4.2 ~ 200 K) dominated by twinning [3, 16].

The facile routes have always been explored to enhance the deformation capacity of metallic alloys [17]. Ultrasonic-assisted processing is to exert dynamic loads on the

target samples with high frequency vibrations (20 kHz ~ 40 kHz), and has already been successfully utilized in the plastic forming and bonding of bulk metallic glasses (BMGs) at room temperature [18-21], achieving fast rejuvenation and structure fabrication under a very low stress. Meanwhile, the acoustic-softening effect of the pure or monocrystal metals has also been discovered and studied from the view of engineering [22, 23]. This feature indicates that ultrasonic loading can be a potential way to change the deformation mechanisms of various materials. However, the engineering studies can't clarify the microstructures-evolution behavior under ultrasonic loading, especially for more complex alloys, such as entropic alloys. In the present work, we tell a new story, and report the discovery of ultrasonic-vibration-enhanced plasticity to almost double the plastic strain of the entropic alloy under a very low stress at room temperature and a relatively-high strain rate of 3×10^{-1} s^{-1} (a compression strain of 30% within 1 s). The microstructures-evolution behaviors and underlying deformation mechanisms are new to the entropic-alloy community. Based on this novel phenomenon, the rapid forming of the entropic-alloy structures in less than 1 second are also proposed, which is of great significance to the extensive applications of these metallic materials.

2. Materials and methods

2.1. Sample preparation

The $Al_{80}Li_5Mg_5Zn_5Cu_5$ (atomic percent, at. %) entropic alloy was produced from elements with a purity of 99.99% in a weight percent by vacuum-induction melting. The ingots were cut into the samples with a diameter of 2 mm and a height of 2 mm by wire-electrical-discharge machining. The entropic-alloy samples were then polished with sandpapers of 2,000 meshes to remove the oxide films on the external surfaces.

2.2. Compression tests

The ultrasonic-compression (UC) experiment was carried out on an ultrasonic-vibration device at room temperature, as schematically presented in Fig. 1a. This device is made of 5 components, including a pneumatic piston, booster, horn, worktable, and power supply. The pneumatic piston converts the air pressure into mechanical pressure to a booster, and the booster converts the electrical energy from the power supply to vibration with a resonant frequency. The ultrasonic system, including the piezoelectric transducer and horn, has a resonant frequency of 20 kHz. Hence, the ultrasonic-loading frequency was set as 20 kHz. The customized ultrasonic horn can amplify the vibration amplitude to a maximum value of 60 μm, and directly exert the loads to the sample. The entropic-alloy sample was put on a dynamometer to receive the real-time force during ultrasonic loading. The data-acquisition card (National Instruments NI-9237) was used to collect and process the force data with a frequency of 2,000 Hz. The ultrasonic vibration was triggered at the applied load of 50 N on the sample. This trigger force is to eliminate the clearance between the ultrasonic horn and sample. Previous experiments show that the deformation stress of the entropic alloy

decreases with increasing the vibration amplitude (Fig. S1), due to the enhancement of the stress-wave effect as the vibration amplitude increases. Therefore, the maximum vibration amplitude (60 μm) has been chosen for the ultrasonic loading to take full advantage of ultrasonic vibration. The UC can achieve cyclic loading with 20,000 cycles within 1 s, and a high instantaneous strain rate reaching 10^3 s^{-1}, which can be estimated by the ratio of the amplitude (60 μm) to sample length (2 mm) within the half vibration period (1/40,000 s). The $Al_{80}Li_5Mg_5Zn_5Cu_5$ entropic alloy achieved a maximum compression strain of 30% within 1 s under the ultrasonic compression. Thus, the average strain rate can be calculated as 3×10^{-1} s^{-1}.

The conventional-compression (CC) experiment was conducted on a mechanical testing machine (Zwick Roell Z050 TEW). The compression strength of the entropic-alloy sample was measured at a stain rate of 2×10^{-4} s^{-1}.

2.3. Thermal imaging

The thermal images of the deformation area of the entropic alloy during UC were captured by the infrared imaging camera (Fotric 280d), and the data-acquisition frequency used in experiments is 21 Hz.

2.4. X-ray diffraction

Phase identification was determined by X-Ray Diffraction (XRD), using the Rigaku miniflex 600 XRD instrument and employing the Cu Kα radiation with a wavelength of 0.154 nm. The XRD pattern was acquired in a scanning angle 2θ range of 20° ~ 90° at a scan rate of 4° per minute and a scan interval of 0.02°.

2.5. Transmission electron microscopy

The samples after deformation were cut in half along the compression axis for the characterization of deformation areas. The microstructure and phase analysis were performed in a transmission electron microscope (TEM, FEI Titan Themis) equipped with the energy dispersive spectroscopy (EDS). The entropic-alloy samples for the TEM observation were prepared on the Dual Beam System (FEI Scios).

2.6. Electron Backscatter Diffraction

The microstructure evolutions in the deformation areas of the samples were characterized by electron backscattered diffraction (EBSD), using the TESCAN MAIA3 scanning electron microscope, equipped with an HKL-EBSD system. The samples were prepared by ion-beam polishing for 1 h at 6.5 kV. The EBSD characterizations were operated with a step size of 0.5 ~ 2 μm at 20 kV, and the Oxford HKL Channel 5 software (Oxford Instruments) was used to analyze the obtained data [8]. The local misorientation of the deformation area was determined, based on a kernel average misorientation (KAM) method [24].

2.7. Ultrasonic-assisted forming

The steel mould was fabricated into a regular hexagon cavity that can be inscribed in a cylinder with a diameter of 2 mm. The $Al_{80}Li_5Mg_5Zn_5Cu_5$ sample with a diameter of 2 mm was placed on the steel mould and was applied with the UC loading at a maximum stress of 98 MPa. Thus, the entropic-alloy sample was formed into the regular hexagon rod by plastic deformation within 1 s. Similarly, the steel mould of

microgrooves with a depth of 200 μm and a width of 400 μm was fabricated by wire-electrical-discharge machining. Then the microgrooves were rapidly patterned on the surface of the entropic alloy by UC.

3. Results

3.1. Compressive-deformation behavior

The $Al_{80}Li_5Mg_5Zn_5Cu_5$ entropic alloy was subjected to the CC and UC at ambient temperature, respectively. Both of the compression tests have been repeatedly conducted for 3 times under the same loading conditions to ensure the repeatability of results (Fig. S2 and S3). As shown in Fig. 1a, the plunger rod of an ultrasonic booster applied the dynamic load on samples with high frequency vibrations (20 kHz) in the UC test. The entropic alloy exhibited a typical compression fracture with large cracks at a strain of 17% in the CC test, while assisted with ultrasonic vibrations, the compression strain of the sample increased to 30% without obvious cracks (Figs. 1b and S4), suggesting that the plasticity of the entropic alloy was obviously enhanced under ultrasonic loading. Due to the vibratory friction, the mean temperature of the deformation area was slightly increased from room temperature to 362 K during ultrasonic loading (Figs. 1c and S5), and the plastic deformation was accomplished within 1 s (Video S1). The influence of this instantaneous thermal effect on plastic deformation can be ignored, considering that it is far below the recrystallization temperature of the entropic alloy. The maximum stress applied in UC is

only 98 MPa at an average strain rate of 3×10^{-1} s^{-1} (Fig. 1e), less than 1/6 of the compressive strength (650 MPa) obtained in CC (Fig. 1d). That is to say, a higher plastic strain of the entropic alloy was achieved in UC under a relative high strain rate and a very low compression stress. The distinct compression behaviors indicate that the underlying deformation mechanisms for this entropic alloy are different at various loading modes.

A series of experiments have been conducted to confirm that this unique deformation behavior is not induced by the accumulation of cracks during ultrasonic loading. The original $Al_{80}Li_5Mg_5Zn_5Cu_5$ samples have been pre-loaded by UC, achieving different samples with a pre-strain of 10%, 20%, and 30%, respectively. Subsequently, the samples with different pre-strains are subjected to the conventional compression at a strain rate of 2×10^{-4} s^{-1} on the mechanical-testing machine. The obtained stress-strain curves are shown in Fig. S6, the maximum deformation stresses reach 648 ~ 680 MPa, which is much higher than the stress under the ultrasonic loading (98 MPa). In addition, the micro hardness of the longitudinal section of the deformed sample with an UC strain of 30% has been measured on the automatic micro-hardness instrument (FM-ARS9000). As shown in Fig. S7, 10 × 20 points distributing in the deformation area (0.8 × 1.6 mm) have been detected, and the micro-hardness of the deformation area is 122 ~ 158 HV, which is higher than the micro-hardness of the original sample (110 ~ 118 HV). This trend can prove that there is no property degradation of the entropic alloy after ultrasonic loading. The electron backscattered

diffraction (EBSD) detection shows no crack in the deformed area of the entropic alloy after ultrasonic loading (Figs. 2g and S8). Meanwhile, the longitudinal sections of the original sample and compressed sample have been observed, respectively, by a scanning electron microscope (SEM), as exhibited in Fig. S9, the conventionally-compressed sample with a strain of 17% demonstrates significant cracking on the longitudinal section (Fig. S9b), while for the ultrasonic-compressed sample with a strain of 30%, there is no crack observed (Figs. S9c, d). Therefore, the significant decrease of deformation stress under ultrasonic loading is due to the unique evolution of microstructures in the entropic alloy rather than the effect of cracks.

3.2. Microstructure characterization

The initial microstructure of the $Al_{80}Li_5Mg_5Zn_5Cu_5$ alloy shows a predominant volume fraction of an FCC α-Al with intermetallic compounds (IMCs) precipitated at grain boundaries (Fig. 2). The X-ray diffraction (XRD) patterns of the samples show the peaks of FCC phases and a series of IMCs [25]. The peak broadening was observed after compression due to lattice distortion (Fig. 2a). The transmission electron microscopy (TEM) characterization coupled with energy dispersive spectroscopy (EDS) reveal that the IMCs phases are rich in Mg, Zn, and Cu elements in addition to the Al element (Figs. 2b, c, d), and these phases exhibit higher strengths and brittleness than the FCC matrix [26]. The electron backscattered diffraction (EBSD) patterns demonstrate the change of the grain size and orientation in the deformation areas. The

longitudinal sections of the samples have been repeatedly observed by EBSD and TEM ensuring a good repeatability of the results. The number of grains with a size of 10 ~ 25 μm accounts for around 60% in the detected areas of the original and CC samples (Figs. 2e, f). However, there still exist coarse grains with the size of 100 ~ 160 μm. In contrast, the coarse grains of FCC phases are refined and thus, disappeared in the UC sample, achieving an average grain size of 17 μm (Figs. 2g and S10). Meanwhile, more bulging grain boundaries are induced after UC (Fig. 2g), which may facilitate boundaries sliding during deformation [27]. Moreover, the large size of IMCs phases (~ 15 μm) is distributed locally in the original samples (Fig. 2h), which is against the cooperative deformation of the adjacent FCC grains. The CC process obtained slightly-refined IMCs with a size of about 12 μm (Fig. 2i), while under the UC, the ultrasonic vibration effectively crushed the IMCs phases into an average size of 6 μm, which dispersed the refined IMCs uniformly at the grain boundaries of FCC phases (Fig. 2j and Fig. S11). The pole figures of the grains in the deformation area of the entropic alloy have been obtained from the EBSD detection (Fig. S8). Comparing with the grain orientations of the original sample (Fig. 2k), the CC process significantly enhanced the deformation texture of the Goss {110}<001> with a maximum pole density of 9.28 (Fig. 2l and Fig. S12). Conversely, the UC undermined the preferential grain orientation during deformation, hence weakening the deformation texture and anisotropy in the entropic alloy (Fig. 2m).

The TEM images of the deformation areas further clarify microstructures evolution

in the entropic alloy under UC. Extensive dislocations and sub-grains are observed in the FCC α-Al phases, and a series of shear bands with a thickness about 120 nm are also formed in the dislocation areas (Fig. 3a), indicating that the FCC phases have undergone large deformation and accommodated the major plastic strain by dislocation glide [27]. The high-resolution images of magnified areas demonstrate the microcracks in the IMCs phases caused by compressive deformation, resulting in the refined IMCs precipitated at grain boundaries of FCC phases (Figs. 3a and S13). The EDS mapping of the refined phases shows the same compositions as that of IMCs (Figs. 2d and S14), which confirms the refinement of IMCs induced by dynamic loading in UC. The rotation behaviors in grain interiors are also estimated under different compression modes. As shown in Fig. 3b, after conventional loading, the Euler angles of crystals inside the grain exhibit a minimal deviation (within 5°) along the orientation, *A*, indicating a slight rotation in grain interiors. However, UC causes a large-angle rotation of internal crystals in a multi-axis (Fig. 3c), thus inducing a significant difference of orientations in grain interiors, which can promote the formation of sub-grains with new orientations. The local misorientation of the grains is adopted to characterize the distribution of dislocations after compression. The densities of geometrically-necessary dislocations (GND) are obtained, based on the strain-gradient theory [28]. The average dislocation density (ρ^{GND}) in the deformation areas has the same order of magnitude under both compression modes. It is notable that the dislocations induced by CC tend to be localized in several grains and grain boundaries (Fig. 3d), which is not conducive to

accommodating plastic deformation [29]. However, under UC, the dislocations distribute more evenly in the deformation area (Fig. 3e), also achieving a higher compression strain. These different microstructure evolutions in the entropic alloy correspond to the distinct deformation mechanisms.

4. Discussion

In the CC, the samples are subjected to the unidirectional loading with a constant strain rate of 2×10^{-4} s^{-1}. When undergoing plastic deformation, the dislocations tend to pile up at grain boundaries and in the IMCs-precipitated areas [30], inducing the dense GND in local regions (Fig. 3d). This deformation behavior achieves a compression strength of 650 MPa (Fig. 1d), due to the dislocations-strengthening effect. However, the stress concentrations are also produced in the dislocations pile-up areas, resulting in crack initiation, propagation, and material fracture eventually [29]. Consequently, a relatively-low deformation strain of 17% was obtained under a high stress in CC (Fig. 1b). By contrast, in UC, the high-frequency cyclic loading (20 kHz) and the high instantaneous strain rate reaching 10^3 s^{-1} that can be estimated by the ratio of the amplitude to sample length within a half vibration period are achieved. These loading features evoke different evolutions of FCC phases and IMCs, as presented schematically in Fig. 4, obtaining a higher plastic strain at a low stress of 98 MPa under UC.

The combination of cyclic loading and high strain rate produces the stress waves in the sample during UC. Therefore, within one loading cycle, when the ultrasonic rod vibrates downward, the high-strain-rate compression induces the rapid glide and multiplication of dislocations, achieving the fast plastic deformation as well as elastic strain in the entropic alloy. Meanwhile, the compressive-stress waves propagate in the material and are reflected at the bottom of the sample, turning to be opposite stress waves [31]. When the ultrasonic rod vibrates backward, the relief of the elastic strain and the reflected stress waves will cause the reverse slip of the partial-deformation areas. Hence, the dislocations-migrating orientations are rearranged due to the altered stress state [32]. This loading mode produces a relaxation effect for the dislocation accumulation, and facilitates the dislocations diffusion, which can suppress the dislocation tangle and pile-up in local regions. Thus, after multiple loading cycles, the dislocations achieve a higher density and distribute more uniformly in the deformation area (Fig. 3e). Similar to the effect of the image force on dislocations [33, 34], dynamic loading preferentially activates the dislocations migrating to the orientations with low resistance, and generates more movable dislocations in the deformation areas [27]. As a result, the work-hardening behavior is significantly diminished during deformation, and higher plastic strains can be achieved at a low stress even less than 1/6 of the compression strength (Fig. 1e).

Therefore, the plastic deformation of the entropic alloy in an ultrasonic-loading cycle involves the competition between dislocations immobilization (entanglement or

pile-up), and the generation of movable dislocations, which is corresponding to work hardening and stress relief, respectively. At the loading stage, the high instantaneous strain rate (up to 10^3 s^{-1}) of stress waves causes the rapid nucleation and multiplication of dislocations in FCC grains, according to the Orowan theory [35], the relationship between the dislocation motion and strain rate can be given as:

$$\frac{d\varepsilon}{dt} = \frac{d\rho_d}{dt} bL + \rho_d bv$$

ε is the deformation strain, ρ_d is the dislocation density, t is loading time, b is magnitude of the Burgers vector, L is the average displacement of a dislocation, and v is the dislocation-gliding velocity.

The dislocation density (ρ_d) in the deformation region increases dramatically, and the dislocations with different Burgers vectors (b) tend to be nucleated and emitted at the initial stage of an ultrasonic loading cycle. While the dislocation-gliding velocity (v) is limited to the sound velocity in the material due to the phonon-drag effects [36], thus the movable dislocations with a confined mean free path (L) cannot effectively accommodate the plastic strain and dissipate the inputting ultrasonic-loading energy, which may induce a risk of embrittlement. However, the average strain of a single ultrasonic-loading cycle is only 1.5×10^{-5} (a maximum strain, 30%, divided by 20,000 loading cycles in 1 s), this loading mode can avoid the dislocations avalanche and crack initiation at a high instantaneous strain rate (up to 10^3 s^{-1}), while generating great amounts of dislocations with different Berger vectors in the deformation region. Then, at the unloading stage, the reflected stress waves will release the tangling and pilling-up

dislocations, and also promote dislocations annihilation by increasing the encounters of the dislocations with opposite Burgers vectors, which suppresses the dislocations pile-up in localized areas (Fig. 3d,e), and significantly reduces the dislocations-motion resistance in a next ultrasonic loading cycle. As the deformation increases, the diffused dislocations from different slip planes inevitably intersect with each other, forming the high dense of forest dislocations (Figs. 3a and S13), and producing stress concentrations in the dislocation walls [37, 38]. However, because of the stress-relief effect of the UC, these dislocation junctions will be driven to merge into grain boundaries [39, 40], leading to the formation of sub-grains boundaries and grain refinement of the coarse FCC phases (Figs. 2g and 3a), which contributes to accommodating dense dislocations and releasing stress concentrations. Thus, the cyclic-stress waves produce a dynamic-recovery effect on the microstructures evolution at ambient temperature, inducing a dramatic reduction of the deformation stress and enhanced plasticity of the entropic alloy under ultrasonic loading.

In addition, different loading modes exhibit distinct stress-transfer mechanisms, and significantly affect the interface interaction of the FCC α-Al phase and IMCs (Al_2Cu, $MgZn_2$) in the entropic alloy. In the conventional quasi-static loading, the stresses tend to distribute uniformly on the FCC-IMCs heterogeneous interfaces [41], the plastic FCC phases preferentially deform according to the minimal energy principle, while the hard IMCs retain integrity and move with the plastic deformation of FCC grains until the work hardening increases to a certain extent, then the IMCs may slightly

fracture due to the increased back stress on the interfaces (Fig. 2i). However, in the ultrasonic loading, the high instantaneous strain rate (up to 10^3 s^{-1}) induces the rapid pile-up of dislocations in the FCC-IMCs interfaces, causing a high back stress on IMCs. Meanwhile, the reflection and refraction of cyclic-stress waves tend to occur on the FCC-IMCs interfaces due to the different acoustic resistance, inducing a high strain rate and intensive stress concentration. Based on the balance between the kinetic energy and the newly-generated surface energy [42], the nominal fragment size of IMCs under dynamic loading can be expressed as:

$$d = \left(\frac{\sqrt{20} K_{Ic}}{\rho c \varepsilon'} \right)^{2/3}$$

K_{Ic} is the material fracture toughness, ρ is the material density, c is the sonic velocity in material, and ε' is the loading stain rate.

Hence, the fragment size decreases with the increase of strain rate, and the high strain rate can induce the fragmentation of brittle phases under a low stress owing to their poor ductility [29]. As observed in Figs. 3a, S13, and S14, the microcracks and debris are more prone to be initiated in IMCs under ultrasonic loading, due to the high back stress of heterostructures at the FCC-IMCs interfaces [41]. And the ruptured and refined IMCs tend to disperse in the FCC grain interiors and boundaries along with the plastic deformation, the refinement and rotation of FCC grains (Figs. 2j, S10, and S11). This evolution can inhibit the excessive pile-up of dislocations around the coarse IMCs embedded at grain boundaries, and is conducive to the cooperative deformation of FCC grains, which could improve the migration ability of grain boundaries, and the refined

IMCs may even be regarded as the solid lubricant [43]. In short, as depicted in Fig. 4, the microstructure evolutions under UC effectively enhance the plasticity of the entropic alloy to achieve the rapid deformation at low stresses.

Furthermore, it is notable that the crystals of the FCC-grain interiors undergo multi-angle rotations under ultrasonic loading (Fig. 3c), which helps accommodate dense dislocations and release stress concentrations during the formation of sub-grain boundaries, thus improving the deformation capacity of samples under cyclic loading [44]. When activated by the recovery stress during the ultrasonic-loading cycles, the dislocations with different Burgers vectors will be rearranged by reverse motions and interactions, such as diffusion, tangle, and annihilation after every ultrasonic-loading cycle, and the dislocations free paths tend to change to the directions with the lowest sliding resistance in the next loading cycle, exhibiting multiple-gliding orientations. The polycrystalline materials are composed of grains with different shapes, sizes, orientations, and boundaries. Thus, the macro-plastic deformation of the entropic alloy need to be obtained by the cooperative deformation of grains with different slip systems. According to the Schmid theory, during the polycrystalline plastic deformation, each grain is required to have at least 5 independent slip systems to meet the requirements of the cooperative deformation [45]. Therefore, there are multiple activated slip systems in the entropic alloy during ultrasonic loading to achieve a plastic strain of 30%. In addition, the Schmid factor in the deformation area of the entropic alloy after ultrasonic loading is obviously higher than that of conventional loading (Fig. S15), demonstrating

that the slip systems tend to be more easily activated under UC. This trend indicates that different slip systems can be activated during ultrasonic loading, which will causes the lattice deflection in FCC grains [10]. Hence, under the constraint of grain boundaries, the crystals of the grain interiors gradually rotate towards different favorable orientations that are conducive to plastic deformation (Fig. 3c), achieving uniform-stress fields [36]. Therefore, the preferential grain orientation is attenuated under UC. This evolution can explain the elimination of deformation textures after ultrasonic loading (Figs. 2m and S12). In contrast, under the conventional loading, the dislocations gliding and grain orientations are highly correlated with the axial loading direction [46], which significantly enhances the Goss {110}<001> deformation textures (Figs. 2l and S12). Besides, the maximum temperature in the deformation areas during ultrasonic loading is only 89℃ (Figs. 1c and S5), no evidence of grain-boundary sliding has been observed at this low temperature. Therefore, the large angle rotation of FCC grains is caused by the dislocations diffusion and lattices deflection under ultrasonic loading.

Figure 5a exhibits the comparison of the deformation behavior under UC in the present work and the conventional compression of entropic alloys (Table S1). It can be seen that most of the conventional-loading tests were conducted under a low strain rate or high temperature to reduce the deformation stress. While the UC of the entropic alloy achieves a very low deformation stress of 98 MPa, less than 1/6 of the compression strength, at a relatively-high strain rate ($3 \times 10^{-1}\ s^{-1}$) under ambient temperatures (Figs.

5b, c). Based on this deformation behavior, the ultrasonic-assisted plastic forming was carried out on the entropic alloy. The three-dimensional (3D) structure of a regular hexagon rod with a height of 1.5 mm was formed from the cylindrical sample with a diameter of 2 mm by UC (Figs. 5d, e). By utilizing the steel mould (Fig. S16), the two-dimensional (2D) structure of microgrooves with a depth of 80 μm were patterned on the entropic-alloy surface under UC (Figs. 5f, g). These structures with different scales were rapidly formed within 1 s under a low stress less than 100 MPa, and achieved a replication rate of over 90%, compared with the mould, demonstrating a facile approach for the plastic forming of the entropic alloy.

5. Conclusions

We have demonstrated the ultrasonic-vibration-enhanced plasticity phenomenon, which almost double the plastic strain of the entropic alloy under a very low stress at room temperature and a relatively-high strain rate of 3×10^{-1} s^{-1}. These macroscopic-deformation behaviors of the entropic alloy correspond to distinct microstructure evolutions under ultrasonic loading. The high-instantaneous strain rate (up to 10^3 s^{-1}) and high-frequency cyclic loading (20,000 Hz) during ultrasonic loading induce stress waves and stress-relief effects in the entropic alloy. This loading mode causes the rearrangement of the stress state and dislocation-slip orientations in the deformation areas, facilitating dislocations diffusion and annihilation, and suppressing the dislocations pile-up in local regions. Meanwhile, the reflection and refraction of

cyclic-stress waves at the FCC-IMCs interface induce intensive stress concentration, causing the significant refinement and dispersion of IMCs phases. This dynamic-recovery effect at ambient temperature also enhances the sub-grain formation and large-angle rotation of FCC grains under ultrasonic loading, which attenuates the preferential grain orientations. These microstructural evolutions in the entropic alloy contribute to reduce the deformation stress to 1/6, and achieve higher plastic strains up to 30% as well as eliminate deformation textures. Benefiting from such a unique discovery, a rapid forming process of entropic alloys is also conducted, based on the ultrasonic-loading approach to make complex and delicate structures.

Data Availability statement

All data needed to make the conclusions in the paper are present in the paper and/or the Supplementary Material. Additional data related to this paper can be requested from the authors.

Supplementary material

Supplementary materials are available for this paper.

Declaration of Competing Interest

The authors declare that they have no known competing financial interests or personal relationships that could have appeared to influence the work reported in this paper.

Acknowledgements

The work was supported by the Key Basic and Applied Research Program of Guangdong Province, China [grant number 2019B030302010], the NSF of China [grant

number 51871157], the Science and Technology Innovation Commission Shenzhen [grant number JCYJ20170412111216258], the National Key Research and Development Program of China [grant number 2018YFA0703605], and the Guangdong Basic and Applied Basic Research Foundation [grant number 2020A1515110390]. P. K. L. very much appreciates the supports from (1) the U.S. Army Office Project [grant number W911NF-13-1-0438 and W911NF-19-2-0049] with the program managers, Drs. Michael P. Bakas, David M. Stepp, and S. Mathaudhu, and (2) the National Science Foundation [grant number DMR-1611180 and 1809640] with the program directors, Drs. Judith Yang, Gary Shiflet, and Diana Farkas. The authors are grateful for the helpful discussion with Dr. Zhuang Liu, and also acknowledge the help of the Electron Microscope Center of Shenzhen University for the Microstructure Observation.

References

1. J. W. Yeh, S. K. Chen, S. J. Lin, J. Y. Gan, T. S. Chin, T. T. Shun, C. H. Tsau, S. Y. Chang, Nanostructured high-entropy alloys with multiple principal elements: novel alloy design concepts and outcomes, Adv. Eng. Mater. 6 (2004) 299-303. https://doi.org/10.1002/adem.200300567

2. B. Cantor, I. T. H. Chang, P. Knight, A. J. B. Vincent, Microstructural development in equiatomic multicomponent alloys, Mater. Sci. Eng. A 375-377 (2004) 213-218. https://doi.org/10.1016/j.msea.2003.10.257

3. B. Gludovatz, A. Hohenwarter, D. Catoor, E. H. Chang, E. P. George, R. O. Ritchie, A fracture-resistant high-entropy alloy for cryogenic applications, Science 345 (2014) 1153-1158. https://doi.org/10.1126/science.1254581

4. Z. Li, K. G. Pradeep, Y. Deng, D. Raabe, C. C. Tasan, Metastable high-entropy dual-phase alloys overcome the strength--ductility trade-off, Nature 534 (2016) 227-230. https://doi.org/10.1038/nature17981

5. D. B. Miracle, O. N. Senkov, A critical review of high entropy alloys and related concepts, Acta Mater. 122 (2017) 448-511. https://doi.org/10.1016/j.actamat.2016.08.081

6. Y. Z. Shi, B. Yang, P. K. Liaw, Corrosion-resistant high-entropy alloys: A review, Metals 7 (2017) 43. https://doi.org/10.3390/met7020043

7. Q. S. Pan, L. X. Zhang, R. Feng, Q. H. Lu, K. An, A. C. Chuang, J. D. Poplawsky, P. K. Liaw, L. Lu, Gradient-cell-structured high-entropy alloy with exceptional strength and ductility, Science 374 (2021) 984-989. https://doi.org/10.1126/science.abj8114

8. P. J. Shi, W. L. Ren, T. X. Zheng, Z. M. Ren, X. L. Hou, J. C. Peng, P. F. Hu, Y. F. Gao, Y. B. Zhong, P. K. Liaw, Enhanced strength–ductility synergy in ultrafine-grained eutectic high-entropy alloys by inheriting microstructural lamellae, Nat. Commun. 10 (2019) 489. https://doi.org/10.1038/s41467-019-08460-2

9. F. L. Wang, G. H. Balbus, S. Z. Xu, Y. Q. Su, J. Shin, P. F. Rottmann, K. E. Knipling, J. C. Stinville, L. H. Mills, O. N. Senkov, I. J. Beyerlein, T. M. Pollock, D. S. Gianola, Multiplicity of dislocation pathways in a refractory multiprincipal element alloy, Science 370 (2020) 95-101. https://doi.org/10.1126/science.aba3722

10. E. Ma, Unusual dislocation behavior in high-entropy alloy, Scr. Mater. 181 (2020) 127-133. https://doi.org/10.1016/j.scriptamat.2020.02.021

11. X. D. Xu, P. Liu, Z. Tang, A. Hirata, S. X. Song, T. G. Nieh, P. K. Liaw, C. T. Liu, M. W. Chen, Transmission electron microscopy characterization of dislocation structure in a face-centered cubic high-entropy alloy $Al_{0.1}$CoCrFeNi, Acta Mater. 144 (2018) 107-115. https://doi.org/10.1016/j.actamat.2017.10.050

12. W. R. Zhang, P. K. Liaw, Y. Zhang, Science and technology in high-entropy alloys, Sci. China-Mater. 61 (2018) 2-22. https://doi.org/10.1007/s40843-017-9195-8

13. W. D. Li, D. Xie, D. Y. Li, Y. Zhang, Y. F. Gao, P. K. Liaw, Mechanical behavior of high-entropy alloys, Prog. Mater. Sci. 118 (2021) 100777. https://doi.org/10.1016/j.pmatsci.2021.100777

14. Z. F. Lei, Y. Wu, J. Y. He, X. J. Liu, H. Wang, S. H. Jiang, L. Gu, Q. H. Zhang, B. Gault, D. Raabe, Z. P. Lu, Snoek-type damping performance in strong and ductile high-entropy alloys, Sci. Adv. 6 (2020) eaba7802. https://doi.org/10.1126/sciadv.aba7802

15. N. T. C. Nguyen, P. A. Rad, P. Sathiyamoorthi, A. Zargaran, C. S. Lee, H. S. Kim, Ultrahigh high-strain-rate superplasticity in a nanostructured high-entropy alloy, Nat. Commun. 11 (2020) 2736. https://doi.org/10.1038/s41467-020-16601-1

16. M. Naeem, H. Y. He, F. Zhang, H. L. Huang, S. Harjo, T. Kawasaki, B. Wang, S. Lan, Z. D. Wu, F. Wang, Y. Wu, Z. P. Lu, Z. W. Zhang, C. T. Liu, X. L. Wang, Cooperative deformation in high-entropy alloys at ultralow temperatures, Sci. Adv. 6 (2020) eaax4002. https://doi.org/10.1126/sciadv.aax4002

17. Z. Li, Z. Y. Huang, F. Sun, X. Li, J. Ma, Forming of metallic glasses: mechanisms and processes, Mater. Today Adv. 7 (2020) 100077. https://doi.org/10.1016/j.mtadv.2020.100077

18. J. Ma, X. Liang, X. Y. Wu, Z. Y. Liu, F. Gong, Sub-second thermoplastic forming of bulk metallic glasses by ultrasonic beating, Sci. Rep. 5 (2015) 17844. https://doi.org/10.1038/srep17844

19. F. Luo, F. Sun, K. S. Li, F. Gong, X. Liang, X. Y. Wu, J. Ma, Ultrasonic assisted micro-shear punching of amorphous alloy, Mater. Res. Lett. 6 (2018) 545-551. https://doi.org/10.1080/21663831.2018.1500399

20. J. Ma, C. Yang, X. D. Liu, B. S. Shang, Q. F. He, F. C. Li, T. Y. Wang, D. Wei, X. Liang, X. Y. Wu, Y. J. Wang, F. Gong, P. F. Guan, W. H. Wang, Y. Yang, Fast surface dynamics enabled cold joining of metallic glasses, Sci. Adv. 5 (2019) eaax7256. https://doi.org/10.1126/sciadv.aax7256

21. F. Sun, B. Wang, F. Luo, Y. Q. Yan, H. B. Ke, J. Ma, J. Shen, W. H. Wang, Shear punching of bulk metallic glasses under low stress, Mater. Des. 190 (2020) 108595. https://doi.org/10.1016/j.matdes.2020.108595

22. Z. H. Yao, G. Y. Kim, Z. H. Wang, L. Faidley, Q. Z. Zou, D. Q. Mei, Z. C. Chen, Acoustic softening and residual hardening in aluminum: modeling and experiments, Int. J. Plasticity 39 (2012) 75-87. https://doi.org/10.1016/j.ijplas.2012.06.003

23. L. C. Zhang, C. H. Wu, H Sedaghat, A note on the applicability of a constitutive model with acoustoplasticity to high strain rate deformation induced by high frequency impacts, Int. J. Impact Eng. 157 (2021) 103977. https://doi.org/10.1016/j.ijimpeng.2021.103977

24. M. Calcagnotto, D. Ponge, E. Demir, D. Raabe, Orientation gradients and geometrically necessary dislocations in ultrafine grained dual-phase steels studied by 2D and 3D EBSD, Mater. Sci. Eng. A 527 (2010) 2738-2746. https://doi.org/10.1016/j.msea.2010.01.004

25. X. Yang, S. Y. Chen, J. D. Cotton, Y. Zhang, Phase stability of low-density, multiprincipal component alloys containing aluminum, magnesium, and lithium, JOM 66 (2014) 2009-2020. https://doi.org/10.1007/s11837-014-1059-z

26. R. X. Li, X. Li, J. Ma, Y. Zhang, Sub-grain formation in Al-Li-Mg-Zn-Cu lightweight entropic alloy by ultrasonic hammering, Intermetallics 121 (2020) 106780. https://doi.org/10.1016/j.intermet.2020.106780

27. U. Messerschmidt, Dislocation dynamics during plastic deformation, Springer Science & Business Media, Berlin, 2010.

28. H. J. Gao, Y. Huang, W. D. Nix, J. W. Hutchinson, Mechanism-based strain gradient plasticity: I. Theory, J. Mech. Phys. Solids 47 (1999) 1239-1263. https://doi.org/10.1016/S0022-5096(98)00103-3

29. A. N. Stroh, The formation of cracks as a result of plastic flow, Proc. R. Soc. A-Math. Phys. Eng. Sci. 223 (1954) 404-414. https://doi.org/10.1098/rspa.1954.0124

30. W. H. Liu, Y. Wu, J. Y. He, T. G. Nieh, Z. P. Lu, Grain growth and the Hall-Petch relationship in a high-entropy FeCrNiCoMn alloy, Scr. Mater. 68 (2013) 526-529. https://doi.org/10.1016/j.scriptamat.2012.12.002

31. L. Wang, Foundations of stress waves, Elsevier, Amsterdam, 2011.

32. H. J. Gao, Y. D. Zhang, Q. Wu, J. Song, K. Wen, Fatigue life of 7075-T651 aluminium alloy treated with vibratory stress relief, Int. J. Fatigue 108 (2018) 62-67. https://doi.org/10.1016/j.ijfatigue.2017.11.011

33. J. D. Eshelby, The force on an elastic singularity, Philos. T. R. Soc. A 244 (1951) 87-112. https://doi.org/10.1098/rsta.1951.0016

34. Z. J. Wang, Q. J. Li, Y. N. Cui, Z. L. Liu, E. Ma, J. Li, J. Sun, Z. Zhuang, M. Dao, Z. W. Shan, S. Suresh, Cyclic deformation leads to defect healing and strengthening of small-volume metal crystals, Proc. Natl. Acad. Sci. USA 112 (2015) 13502-13507. https://doi.org/10.1073/pnas.1518200112

35. D. Hull, D. J. Bacon, Introduction to dislocations, Butterworth-Heinemann, 2001.

36. E. Nadgornyi, Dislocation dynamics and mechanical properties of crystals, Prog. Mater. Sci. 31 (1988) 1-530. https://doi.org/10.1016/0079-6425(88)90005-9

37. Y. Hu, L. Shu, Q. Yang, W. Guo, P. K. Liaw, K. A. Dahmen, J. M. Zou, Dislocation avalanche mechanism in slowly compressed high entropy alloy nanopillars, Commun. Phys. 1 (2018) 1-8. https://doi.org/10.1038/s42005-018-0062-z

38. Q. Q. Ding, Y. Zhang, X. Chen, X. Q. Fu, D. K. Chen, S. J. Chen, L. Gu, F. Wei, H. B. Bei, Y. F. Gao, M. R. Wen, J. X. Li, Z. Zhang, T. Zhu, R. O. Ritchie, Q. Yu, Tuning element distribution, structure and properties by composition in high-entropy alloys, Nature 574 (2019) 223-227. https://doi.org/10.1038/s41586-019-1617-1

39. H. Mughrabi, Dislocation wall and cell structures and long-range internal stresses in deformed metal crystals, Acta Metall. 31 (1983) 1367-1379. https://doi.org/10.1016/0001-6160(83)90007-X

40. R. Madec, B. Devincre, L. P. Kubin, From dislocation junctions to forest hardening, Phys. Rev. Lett. 89 (2002) 255508. https://doi.org/10.1103/PhysRevLett.89.255508

41. D. E. Grady, Local inertial effects in dynamic fragmentation, J. Appl. Phys. 53 (1982) 322-325. https://doi.org/10.1063/1.329934

42. Y. T. Zhu, K. Ameyama, P. M. Anderson, I. J. Beyerlein, H. J. Gao, H. S. Kim, E. Lavernia, S. Mathaudhu, H. Mughrabi, R. O. Ritchie, N. Tsuji, X. Y. Zhang, X. L. Wu, Heterostructured materials: superior properties from hetero-zone interaction, Mater. Res. Lett. 9 (2021) 1-31. https://doi.org/10.1080/21663831.2020.1796836

43. A. Hasnaoui, H. V. Swygenhoven, P. M. Derlet, Cooperative processes during plastic deformation in nanocrystalline fcc metals: A molecular dynamics simulation, Phys. Rev. B 66 (2002) 184112. https://doi.org/10.1103/PhysRevB.66.184112

44. Q. Zhu, G. Cao, J. W. Wang, C. Deng, J. X. Li, Z. Zhang, S. X. Mao, In situ atomistic observation of disconnection-mediated grain boundary migration, Nat. Commun. 10 (2019) 1-8. https://doi.org/10.1038/s41467-018-08031-x

45. E. Schmid, W. Boas, Plasticity of Crystals, Hughes, London, 1950.

46. S. Mishra, M. Suresh, A. M. More, A. Bisht, S. Suwas, Texture control to reduce yield strength anisotropy in the third generation aluminum-copper-lithium alloy: Experiments and modeling, Mater. Sci. Eng. A 799 (2021) 140047. https://doi.org/10.1016/j.msea.2020.140047

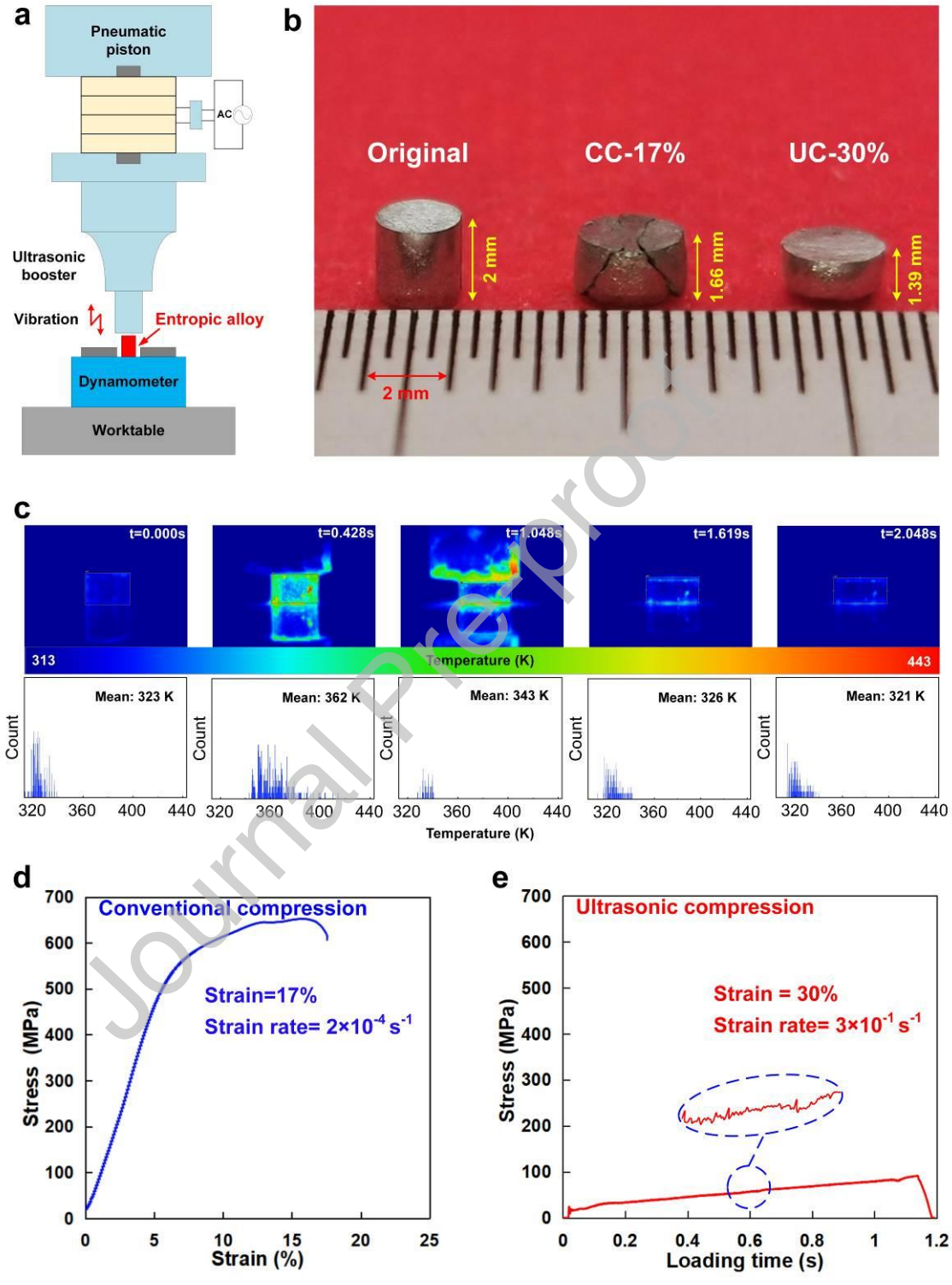

Figure 1. Deformation behavior under different loading conditions. a Schematic of ultrasonic-assisted loading, **b** Sample deformation of conventional compression (CC) and ultrasonic compression (UC), **c** Thermal infrared images of the deformation area during ultrasonic loading, **d** Stress-strain curve of CC at room temperature, **e** Mechanical response of the entropic alloy under UC.

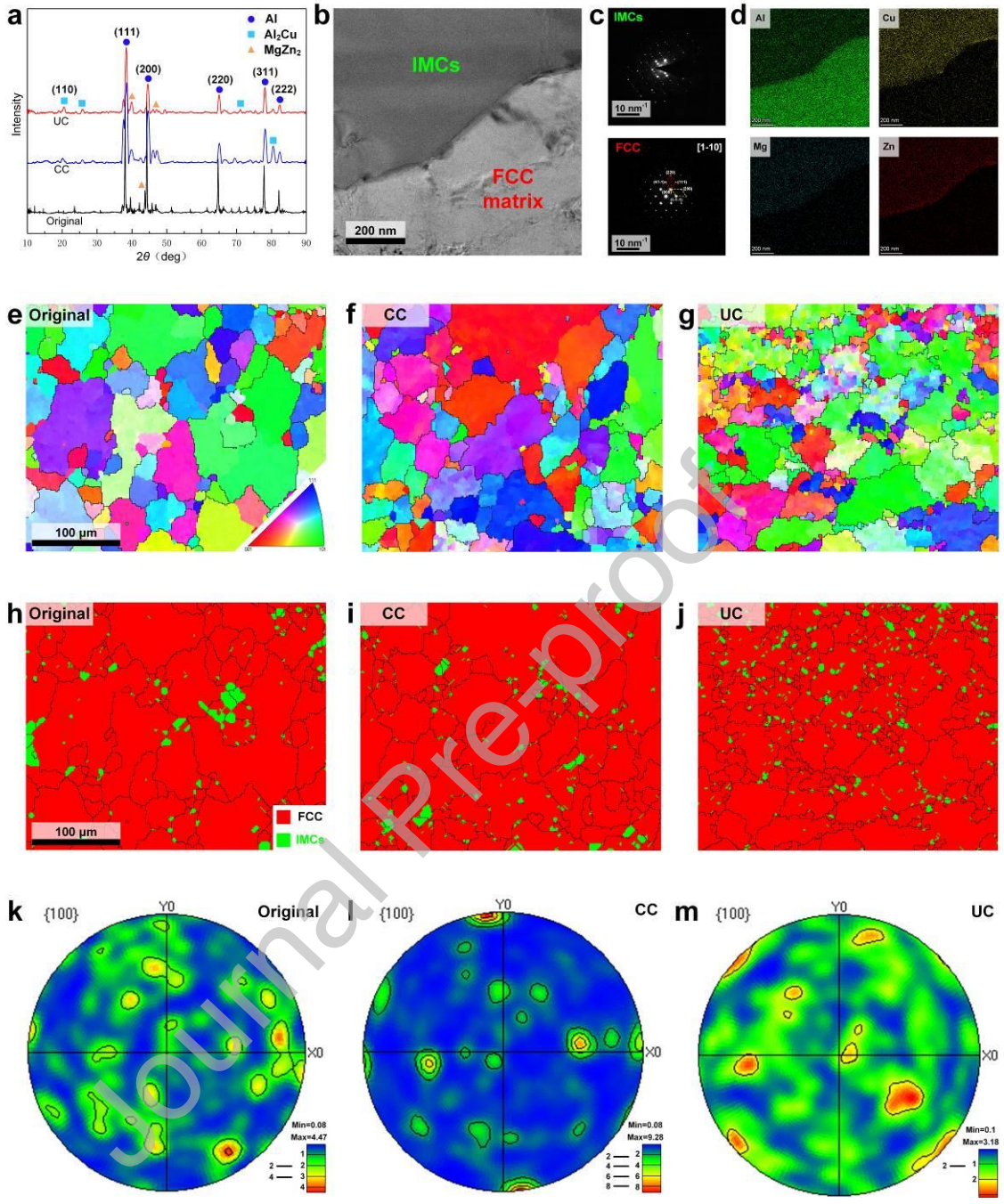

Figure 2. Microstructure analysis of different samples. a X-ray diffraction (XRD) patterns of the original and compressed samples, **b** Transmission Electron Microscopy (TEM) images of different phases, **c** Selected Area Electron Diffraction (SAED) patterns of FCC and IMCs phases, **d** Energy dispersive spectroscopy (EDS) maps of different phases, **e, f, g** Electron Backscatter Diffraction (EBSD) map of the original, CC and UC samples, respectively, **h, i, j** Phase maps of the samples under different loading conditions, **k, l, m** Pole maps of the deformation areas of corresponding samples along the planar {100} direction.

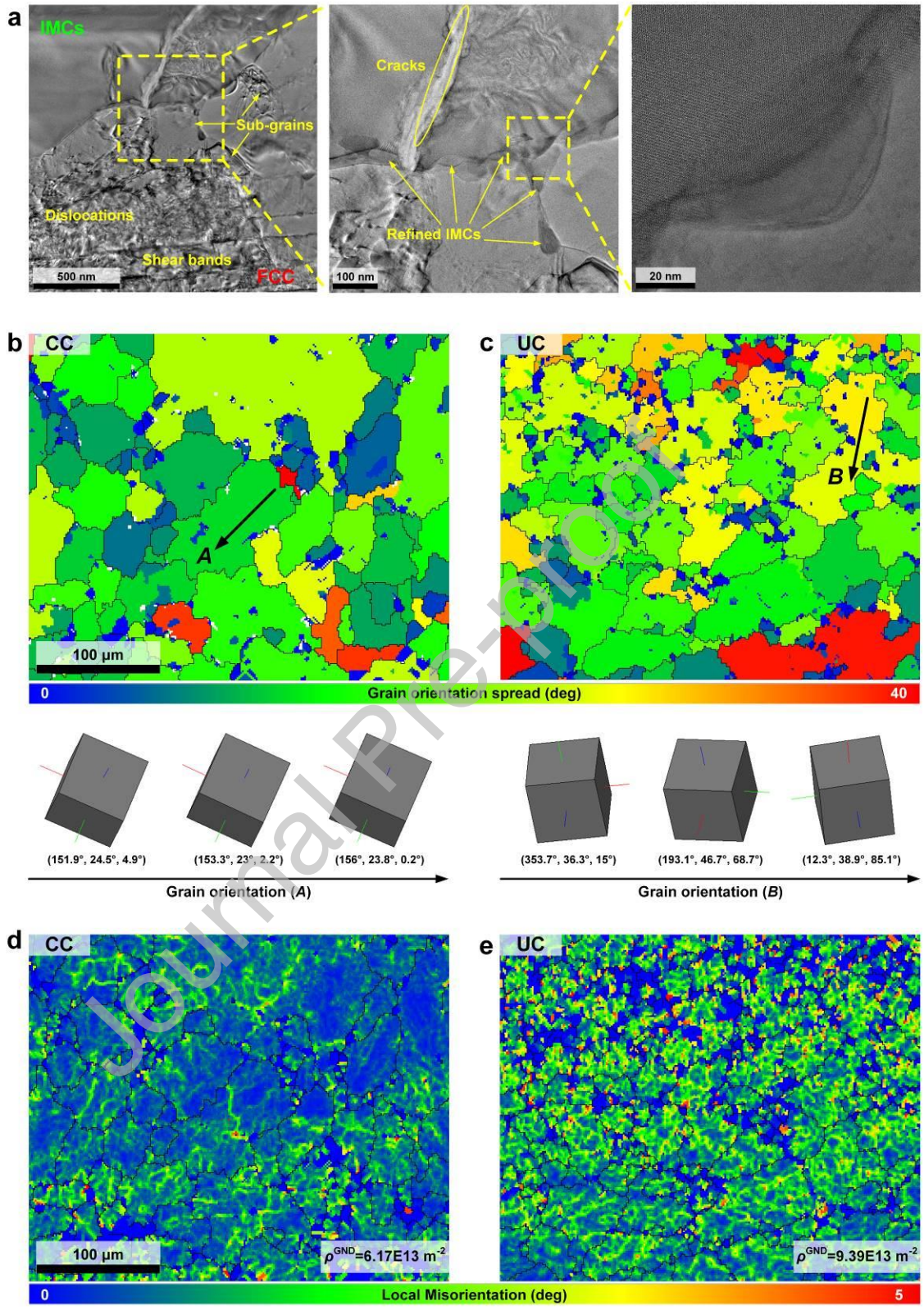

Figure 3. Microstructure evolution under compression. a TEM images of the deformation area in ultrasonic compression, a series of sub-grains, dislocations, and shear bands are formed in the FCC phases due to the accommodation of the plastic strain, and the magnified images demonstrate the microcracks in IMCs phases and the refined IMCs resulted by dynamic loading, **b, c** Grain-orientation spread and internal crystal rotation caused by different loading modes, a small deviation of Euler angles within 5° in the crystals is observed along the orientation, *A*, after conventional loading, while the large-angle rotation of internal crystals in a multi-axis along the orientation, *B*, is induced by ultrasonic loading, **d, e** Distributions of local misorientations corresponding to geometrically necessary dislocations (GND) in the deformation areas induced by compression, the average dislocation density (ρ^{GND}) reaches the same order of magnitude ($10^{13}\,m^{-2}$) under both loading modes, while comparing with the localized dislocations after conventional loading, a more uniform distribution of dislocations is achieved after ultrasonic loading.

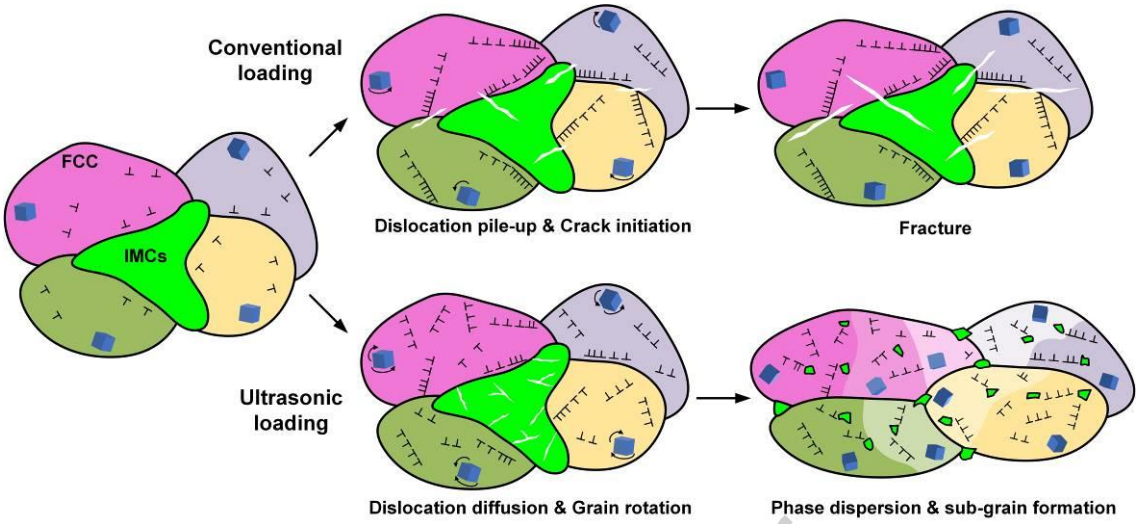

Figure 4. Schematic of microstructure evolution and deformation mechanisms under different loading modes.

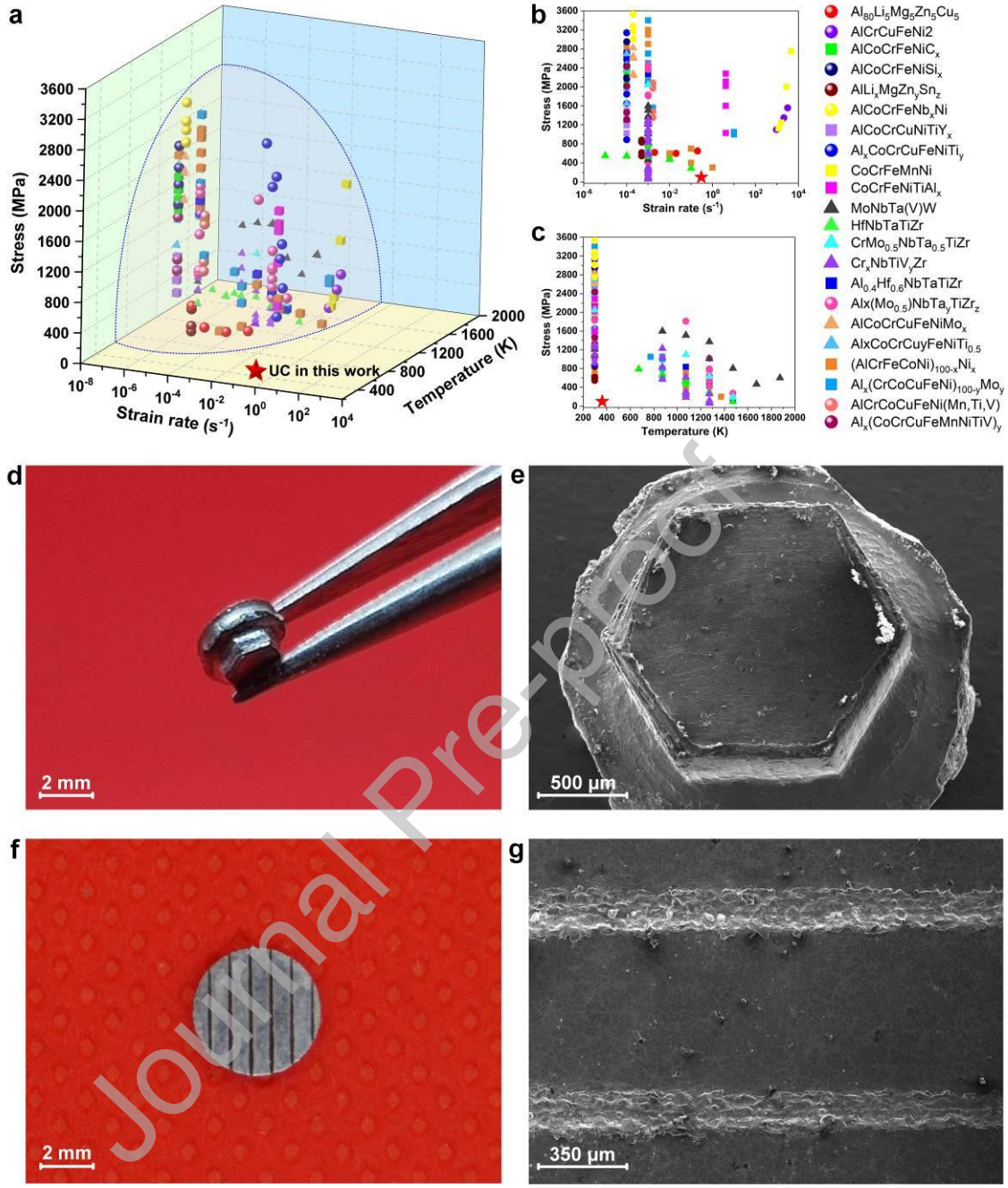

Figure 5. Compression behavior of ultrasonic loading in the present work, compared with the conventional loading of entropic alloys. a Comparison of the strain rate, temperature, and stress under ultrasonic compression and conventional compression, **b** Corresponding relationship between the strain rate and compression stress of entropic alloys, **c** Corresponding relationship between the loading temperature

and compression stress under different loading modes. **Structural plastic forming of the $Al_{80}Li_5Mg_5Zn_5Cu_5$ entropic alloy by ultrasonic loading. d** Regular hexagon rod with a height of 1.5 mm formed from the cylindrical sample with a diameter of 2 mm, **e** The SEM image of the formed regular hexagon rod of the entropic alloy, **f** The microgrooves patterned on the surface of the entropic alloy with a depth of 80 μm and a width of 170 μm, **g** The SEM image of the formed microgrooves on the entropic alloy.

Graphical abstract